Additive Manufacturing 93 (2024) 104445

Contents lists available at ScienceDirect

Additive Manufacturing

journal homepage: www.elsevier.com/locate/addma

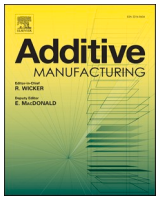

Significant creep-strength improvement in modified 9Cr-1Mo steel via microstructural control through laser powder bed fusion

Tomotaka Hatakeyama *, Kota Sawada, Masahiro Kusano, Makoto Watanabe

Research Center for Structural Materials, National Institute for Materials Science, 1-2-1, Sengen, Tsukuba, Ibaraki 305-0047, Japan

ARTICLE INFO

Keywords:
Laser powder bed fusion
Ferritic steels
δ-ferrite
Creep
Precipitation

ABSTRACT

Modified 9Cr-1Mo steel was manufactured using laser powder bed fusion (LPBF). The as-built LPBF-sample microstructure comprised columnar δ-ferrite grains and fine martensite grains. The δ-ferrite was a unique phase that formed under the significantly rapid LPBF-induced solidification. Creep testing was performed for the LPBF sample at 923 K for up to 10,000 h. The LPBF-sample time-to-rupture and minimum creep rate were at least 10 times longer and 100 times smaller, respectively, than those of conventional modified 9Cr-1Mo steels at 923 K under 100 MPa. Microstructural characterization of the creep-ruptured samples revealed that creep deformation preferentially occurred in the martensite. Thus, the δ-ferrite contributed significantly to the enhanced creep strength. The intrinsic creep resistance of the δ-ferrite phase exceeded that of the martensite. The microstructural stability of the δ-ferrite grains (attributed to dense MX-phase precipitation at the grain boundary) was a likely strengthening factor. Overall, the modified 9Cr-1Mo steel creep strength was successfully improved via unique microstructural control through LPBF. This achievement is expected to extend LPBF application as a novel microstructural control process for steels and alloys, avoiding the diffusional transformation kinetics that occur in conventional heat-treatment processes.

1. Introduction

Laser powder bed fusion (LPBF) is a promising additive manufacturing technique for structural metallic components, and it has advantages such as near-net shaping of complex-shaped products and potential property enhancement through the formation of unique microstructures [1]. However, the long-term reliability of LPBF materials (e.g., their creep properties) for standardization and practical high-temperature applications has not been sufficiently evaluated.

Modified 9Cr-1Mo steel (ASME Grade 91) is a ferritic/martensite heat-resistant steel widely used in boiler tubes and pipes in ultra-supercritical power plants [2]. The microstructure of the steel is controlled as a tempered martensite microstructure via normalization and tempering heat treatments, which yield excellent creep performance. This steel has likely application in next-generation nuclear power reactors owing to its excellent mechanical, corrosion, and irradiation resistance properties [3]. Furthermore, the application of additively manufactured ferrite/martensite steel in nuclear components is being discussed [4–8].

LPBF of ferritic/martensite heat-resistant steels has been attempted [7–14]. Hatakeyama et al. [14] investigated the microstructural development of LPBF-manufactured modified 9Cr-1Mo steel, reporting a δ-ferrite/martensite duplex microstructure in the as-built samples. They concluded that the significantly rapid cooling rate achieved via LPBF causes δ-ferrite solidification in the melt pool without diffusional transformation. The martensite is obtained through the δ-ferrite → austenite (γ) → martensite (α') solid-state phase transformation in the heat-affected zone around the melt pool due to repeated laser scanning.

The mechanical properties of LPBF-manufactured as-built ferritic/martensite heat-resistant steels with duplex microstructures have been investigated and compared with those of wrought steels. Jiang et al. [12] achieved an outstanding tensile-strength/elongation combination at room temperature (RT) through process optimization for reduced-activation ferritic/martensitic steels. Eftink et al. [10] reported enhanced tensile strength for modified 9Cr-1Mo steel at RT, 573 K, and 873 K. For a modified 9Cr-1Mo steel specimen with 13.3-mm gauge length, 3.1-mm width, and 3-mm thickness, Atwani et al. [9] obtained enhanced creep strength within 100 h at 923 K. However, to the best of

* Corresponding author.
E-mail addresses: hatakeyama.tomotaka@nims.go.jp (T. Hatakeyama), sawada.kota@nims.go.jp (K. Sawada), kusano.masahiro@nims.go.jp (M. Kusano), watanabe.makoto@nims.go.jp (M. Watanabe).

https://doi.org/10.1016/j.addma.2024.104445
Received 30 April 2024; Received in revised form 25 August 2024; Accepted 17 September 2024
Available online 18 September 2024

our knowledge, the longer-term creep properties of LPBF-manufactured ferritic/martensite heat-resistant steels have not been reported.

In the long term, conventionally manufactured modified 9Cr-1Mo steel experiences creep-strength degradation [15], one cause of which is preferential martensite recovery at the prior austenite grain boundary [16]. Microstructural degradation through coarsening of the subgrains or $M_{23}C_6$ (M is mainly Cr) or MX (M is mainly V and Nb) precipitate, and through phase transformation from the MX to Z phase, also reduce the creep resistance [17]. Owing to microstructural degradation, the stress exponent of the stress vs. time-to-rupture curve differs from the short to long term [18,19]. Thus, the long-term creep strength must be evaluated to optimize LPBF parameters of heat-resistant materials for high-temperature applications.

In this study, long-term creep testing of LPBF-manufactured modified 9Cr-1Mo steel is performed for up to 10,000 h following the National Institute for Materials Science (NIMS) Creep Data Sheet procedures [20], for a standard specimen geometry with 6-mm gauge diameter and 30-mm gauge length. The creep strength is reliably evaluated through comparison with the reference data for conventional modified 9Cr-1Mo steels in the NIMS Creep Data Sheet [15]. The microstructures of the creep-ruptured specimens are analyzed, and the creep deformation behavior of the LPBF sample, which has a δ-ferrite and martensite duplex microstructure, is discussed.

2. Experimental procedure

A powder with a chemical composition corresponding to modified 9Cr-1Mo steel specifications [21] was produced through gas atomization (Table 1). The average powder particle size (d_{50}) was 40.9 μm. LPBF was performed on 100×100 mm^2 base plate using an SLM 280 3D printer (SLM Solutions) under an Ar flow with the parameters shown in Table 2. Among the four suggested optimal parameter sets, this parameter yielded the highest martensite volume fraction and Vickers hardness in the as-built sample with no porosity [14]. The energy density was calculated as $E = P/vhd$, where P, v, h, and d are the laser power, scan speed, hatch distance, and layer thickness, respectively. The specimen size was φ15 × 90 mm (Fig. 1). These cylinders were removed from the base plate and machined to creep specimens with 6-mm gauge diameter and 30-mm gauge length in the longitudinal direction; the loading direction was parallel to the build direction. Chemical composition of the as-built sample was analyzed and listed in Table 1. Creep tests of the as-built sample were performed in air at 923 K under constant loads of 220, 180, 120, and 100 MPa. Creep tests on ASME Grade 91 steel tubes (T91, NIMS reference code: MGA, MGB, MGC, MGD, MGF, and MGG) were also performed at 923 K for comparison. The chemical composition of the steels is listed in Table 1. The creep-test experiment details are given in NIMS Creep Data Sheet No. 43 A [15].

Table 2
LPBF parameters.

Laser power, P [W]	Scan speed, v [mm/s]	Rotation angle [degree]	Hatch distance,h [mm]	Layer thickness, d [mm]	Energy density, E [J/mm^3]
300	800	67	0.1	0.03	125

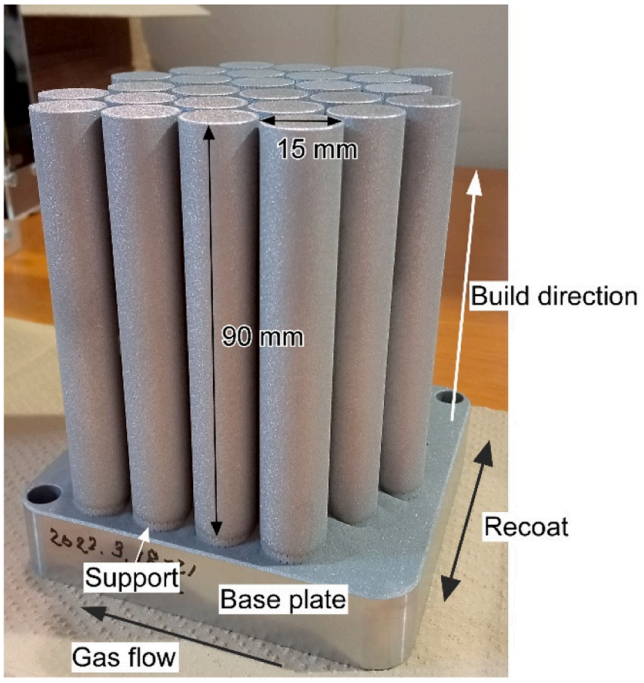

Fig. 1. Appearance of the specimens manufactured by LPBF.

The sample surface parallel to the build direction (stress direction) were finished through chemical—mechanical polishing using colloidal silica for scanning electron microscopy (SEM), electron backscatter diffraction (SEM-EBSD), and Vickers hardness tests. SEM (Auriga Laser, ZEISS) was performed with 15 and 25 kV accelerating voltage using a

Table 1
ASME Grade 91 steel specifications [21], chemical composition of gas-atomized powder, LPBF sample, and reference T91 steel, MGD heat [15] (mass%).

	C	Si	Mn	P	S	Ni	Cr	Mo
ASME Grade 91 Steel Specification	0.07–0.14	0.20–0.50	0.30–0.60	≦0.020	≦0.010	≦0.40	8.0–9.5	0.85–1.05
Powder	0.10	0.38	0.47	0.006	0.002	0.06	8.8	0.95
LPBF	0.09	0.37	0.42	0.006	0.003	0.07	8.86	0.95
MGA	0.10	0.38	0.40	0.015	0.001	0.12	8.53	0.96
MGB	0.09	0.34	0.45	0.015	0.001	0.20	8.51	0.90
MGC	0.09	0.29	0.35	0.009	0.002	0.28	8.70	0.90
MGD	0.10	0.29	0.41	0.010	0.001	0.10	8.41	0.90
MGF	0.11	0.25	0.42	0.013	0.001	0.06	8.41	0.91
MGG	0.10	0.38	0.37	0.018	0.002	0.12	8.60	0.95
	Al	Ti	V	Nb	Zr	Fe	N	O
ASME Grade 91 Steel Specification	≦0.02	≦0.01	0.18–0.25	0.06–0.10	≦0.01	-	0.030–0.070	-
Powder	<0.01	<0.01	0.25	0.09	<0.01	Bal.	0.06	-
LPBF	<0.01	<0.01	0.24	0.09	<0.01	Bal.	0.05	0.01
MGA	0.014	< 0.001	0.21	0.076	< 0.001	Bal.	0.050	-
MGB	0.016	0.001	0.205	0.076	< 0.001	Bal.	0.042	-
MGC	0.001	< 0.001	0.22	0.072	< 0.001	Bal.	0.044	-
MGD	0.016	0.001	0.185	0.07	<0.001	Bal.	0.048	-
MGF	0.001	0.006	0.20	0.08	< 0.001	Bal.	0.053	-
MGG	0.002	< 0.001	0.190	0.08	< 0.001	Bal.	0.0458	-

secondary electron (SE) and external backscattered electron (BSE) detector, respectively. SEM-EBSD (Orion camera, EDAX) was performed with 15 kV accelerating voltage. Vickers hardness tests (HV-100, Mitsutoyo) were performed under a 10-kgf load at five points. The maximum and minimum values were removed, and the average value for the remaining three points was used for evaluation. The sample surface parallel to the build direction were finished through mechanical polishing using alumina for time-of-flight secondary ion mass spectroscopy (TOF-SIIMS) and electron probe micro analyzer (EPMA). TOF-SIMS (TOF-SIMS5, ION-TOF) was performed using Bi_1^+ ion beams with 30 kV accelerating voltage. EPMA (JXA-iHP200F, JEOL) was performed with 7 kV accelerating voltage. Thin foils for scanning transmission electron microscopy (STEM) were prepared from the as-built samples and gauge portions of creep-ruptured samples via electrochemical polishing. STEM and electron-dispersive spectroscopy (STEM-EDS; JEM-2800, JEOL and HD-2700, Hitachi High-Tech) were performed with 200 kV accelerating voltage.

3. Results

3.1. As-built microstructure

Fig. 2(a) is an SEM-BSE image of the as-built sample. The build direction is from bottom to top. No porosity was observed in the microstructure; consequently, a relative density of approximately 100 % was achieved. Columnar δ-ferrite and fine martensite grains are visible (41 % and 59 % volume fractions, respectively [14]), which formed at the melt pool and heat-affected zone, respectively [14]. Fig. 2(b) is an inverse pole figure (IPF) map overlaid on an IQ map of the points indexed as bcc. The orientation parallel to the build direction is shown in the IPF map. The columnar δ-ferrite grains are recognizable but the fine martensite grains are unclear because of the poor IQ value at the martensite in this resolution. Fig. 2(c)–(e) are pole figures produced via orientation imaging microscopy (EBSD-OIM); the texture of the <001>// build direction was formed by the LPBF [14]. Fig. 2(f) and (g) are IQ+ IPF maps of the points indexed as bcc and fcc, respectively, obtained from the box labeled "f" in Fig. 2(b) with higher-magnification and resolution. A hierarchical lath martensitic structure can be recognized in Fig. 2(f). In addition, retained γ grains are observed at the interface between δ-ferrite and martensite in Fig. 2(g).

Fig. 3(a) is a high-magnification BSE image of the central view in Fig. 2(a). Fig. 3(b) is a higher-magnification image of the "b" region in Fig. 3(a). A striped contrast is notable in the δ-ferrite phase. These are dislocations visualized based on the electron channeling contrast [22–24], which appear to be elongated perpendicular to the melt pool boundary. Several spherical particles are visible along the brighter stripe contrast (Fig. 3(b), arrowheads). Orientation analysis for "c" in Fig. 3(a) was performed using SEM-EBSD. The IPF map (Fig. 3(c)) shows the orientation parallel to the build direction. The black-colored grains are retained γ grains formed by the LPBF thermal cycles [14]. Indexing of the Fig. 3(b) area failed because of the poor electron backscattered pattern (EBSP), which was due to significant contamination after long-term electron beam exposure. Fig. 3(d) shows the <001> stereographic projection for "d," the grain of which is identical to the Fig. 3(b) region; hence, the stripe is elongated parallel to the <001> direction (Fig. 3(b), arrow).

The STEM—bright-field (BF) image of the δ-ferrite phase (Fig. 3(e)) confirms a cellular dislocation structure similar to that of the SEM-BSE image. Fig. 3(f)—(h) are Cr, Si, and Nb STEM-EDS maps, respectively. Cr segregation at the high-dislocation-density region was confirmed (Fig. 3(e, f), arrows). Additionally, Si-, Mn-, and O- (not shown here) enriched particles were observed along the segregated region (Fig. 3(e, g, h)). These are considered to be Mn-enriched SiO_2 [25] or $MnSiO_3$ rhodonite particles, [26] as observed in LPBF-manufactured austenitic steels. As shown in Table 1, O concentration of the as-built sample is 0.01 mass%. The O was likely contaminated from the powder or

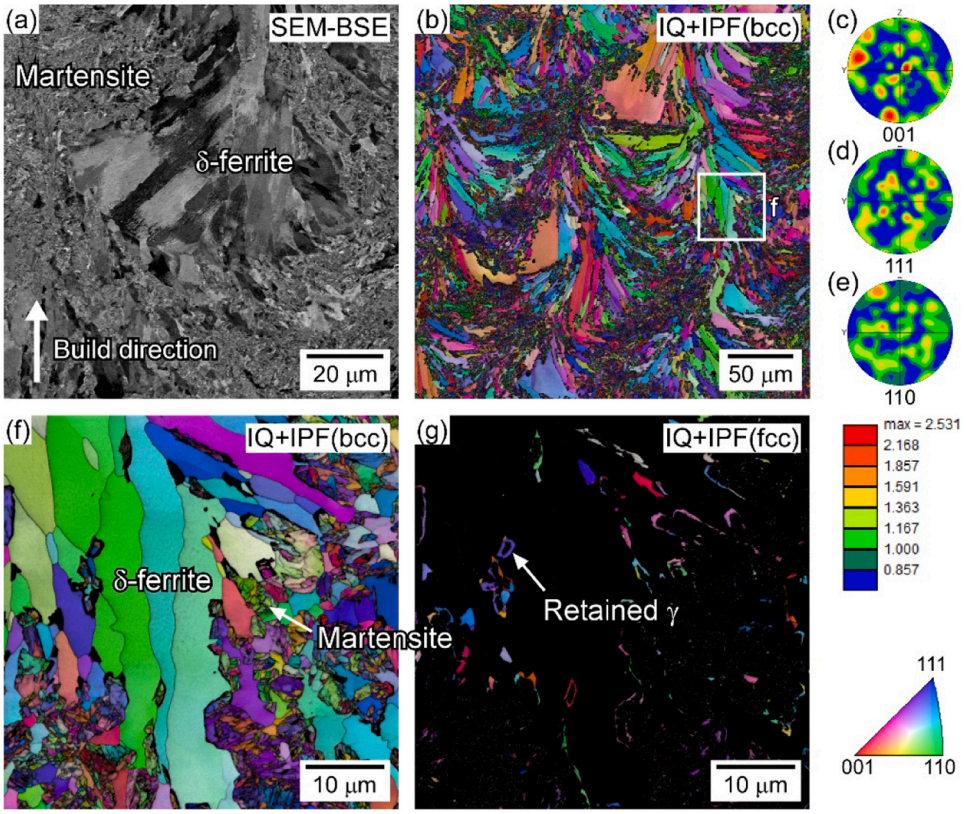

Fig. 2. (a) BSE image, (b) IQ+IPF map of bcc grains, (c) 001, (d) 111, and (e) 110 stereographic projections, IQ+IPF maps of (f) bcc and (g) fcc grains of as-built sample.

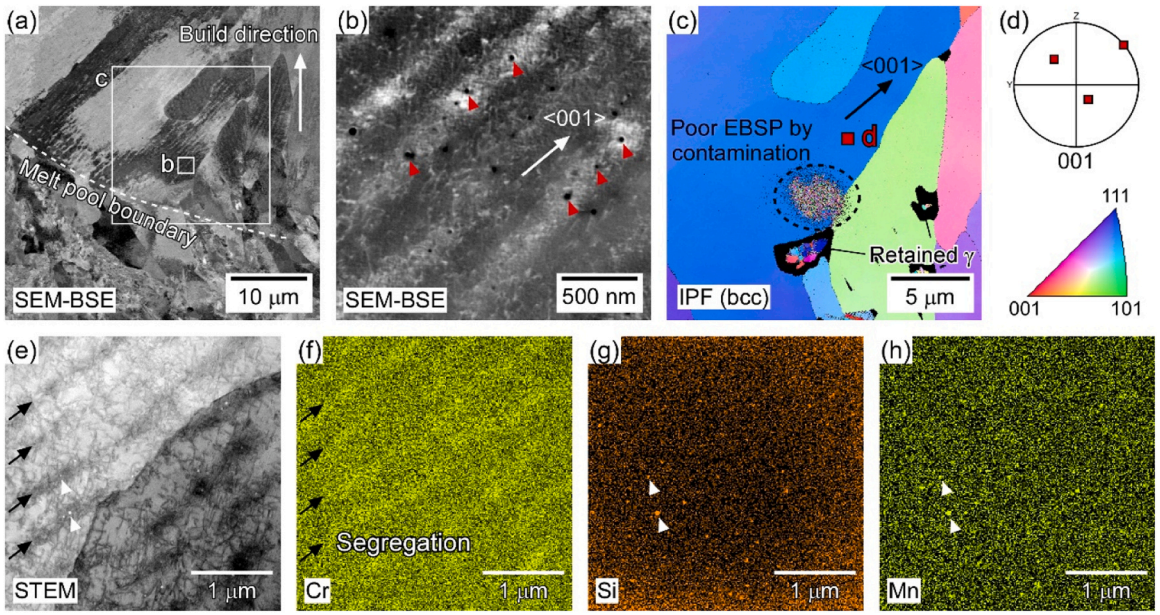

Fig. 3. (a)(b) SEM-BSE images, (c) IPF map for bcc, (d) stereographic projection of "d" point in (c), (e) STEM image, and (f) Cr, (g) Si, and (h) Nb STEM-EDS maps for as-built sample.

environment during LPBF [27]. Nevertheless, the oxide formation from contaminating O suggests potential for in-situ manufacturing of oxide dispersion strengthened steels or alloys [28].

The solidification direction in a melt pool is perpendicular to its boundary [1]. The columnar-grain solidification direction in the as-built sample was parallel to the <001> direction of the bcc lattice [14], indicating segregation and dislocation cell structures were formed during solidification. The formation of cellular structures with segregation along <001> has been observed in austenitic steels and is thought to contribute to strengthening [25,29,30].

Fig. 4(a) and (b) show a STEM-BF image and STEM-EDS map of Cr, respectively, around the δ-ferrite-phase triple junction of the as-built sample. δ-ferrite and martensite were identified based on their microstructural morphologies. Precipitation of a Cr-containing phase with a diameter of tens of nanometers was observed at the grain boundary. This was likely due to high-temperature exposure in the heat-affected zone around the melt pool during LPBF. Spherical Si-rich oxide particles are visible in the grain interior (Fig. 3). Fig. 4(c) and (d) are a STEM-BF image and STEM-EDS map of Cr, respectively, on the martensite. The lath width was estimated to be on the order of hundreds of nanometers. No segregation or precipitation of Cr or other strengthening elements (Mo, V, or Nb) was observed. However, spherical Si-oxide particle precipitation was confirmed, as for the δ-ferrite phase. This martensite was formed via the δ → γ → α' phase transformation at the melt-pool heat-affected zone by the LPBF thermal cycle [14]. Therefore, the Si oxide observed in the martensite likely nucleated in the δ-ferrite and was preserved during the solid-state phase transformation.

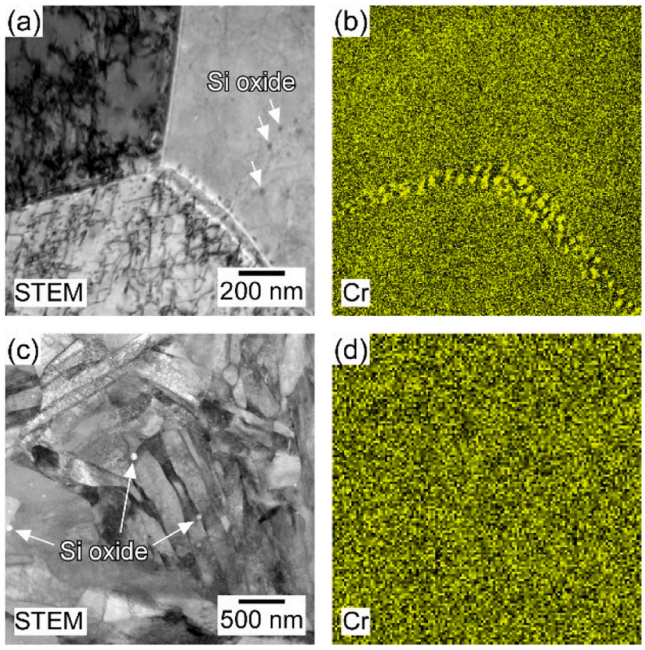

Fig. 4. (a)(c) STEM-BF images and (b)(d) STEM-EDS maps of Cr taken (a)(b) around the δ-ferrite-phase triple junction and (c)(d) at the martensite of as-built sample.

Fig. 5(a) and (b) show a scanning ion microscope (SIM) image and a C^- (m/z: 12) map obtained by TOF-SIMS of the as-built sample. A higher carbon concentration in the martensite and martensite/δ-ferrite interface than in the δ-ferrite was qualitatively confirmed. Fig. 5(c) and (d) show BSE images of the as-built sample. Line profiles of carbon concentration along lines 1 and 2 in Fig. 5(c) and (d), obtained by EPMA, are shown in Fig. 5(e). Although martensite and δ-ferrite are difficult to distinguish from each other solely from the BSE image because of the poor channeling contrast owing to the surface and beam conditions optimized for EMPA analysis, it was suggested that higher and lower carbon concentrations correspond to martensite and δ-ferrite, respectively. This revealed that the carbon concentration in the δ-ferrite is approximately 0.04 mass%.

3.2. Creep properties

Fig. 6(a) shows the relationship between stress and time-to-rupture of the LPBF sample. Note that 100-MPa creep testing is currently in progress. The data for T91 steel tubes (NIMS reference code: MGA, MGB, MGC, MGD, MGF, and MGG heats) reported in the NIMS Creep Data Sheet [15] were also plotted for comparison. The LPBF-manufactured modified 9Cr-1Mo steel exhibited significantly enhanced creep strength compared to the conventional sample for at least 10,000 h. The LPBF-sample time-to-rupture exceeded that of the T91 steel by more than 10 times under 100 MPa at 923 K. Although the LPBF-sample stress

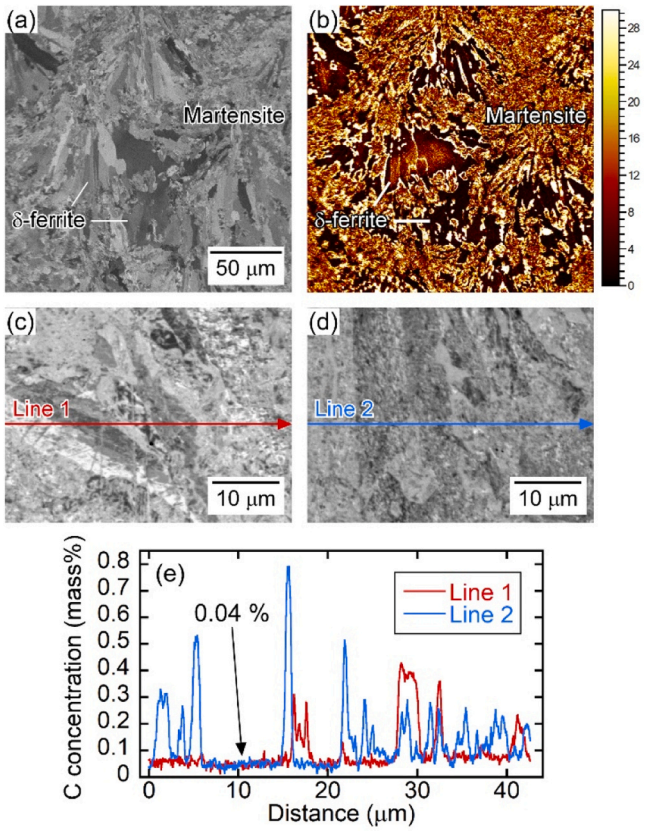

Fig. 5. (a) SIM image, (b) C^- (*m/z*: 12) map obtained by TOF-SIMS, (c)(d) BSE image, and (e) line profile of the carbon concentration along lines 1 and 2 in (c) and (d) measured by EPMA from as-built sample.

vs. time-to-rupture slope was steeper than that of the T91 steel, no remarkable premature failure was observed for the former until 10, 000 h.

Fig. 6(b) and (c) show the elongation and reduction of area of the LPBF sample against the time-to-rupture, respectively. The values reported in the NIMS Creep Data Sheet [15] were also plotted for comparison. The elongation of the LPBF sample on the short-term side was less than that of the conventional steel, but comparable at a time to rupture of ~4000 h. The reduction of area of the LPBF sample was comparable to that of conventional steel. Thus, the modified LPBF-manufactured 9Cr-1Mo steel had sufficient ductility, although some LPBF-manufactured steels and alloys exhibit poor creep ductility [31–33].

Fig. 7 shows the creep strain vs. time, creep rate vs. time, and creep rate vs. strain curves of the as-built sample obtained at 923 K under 220, 180, 120, and 100 MPa. Creep testing at 100 MPa is currently in progress. The curves for MGD with identical time-to-rupture at 923 K (110, 100, 70, and 60 MPa) were drawn for comparison. Comparing the strain and creep-rate vs. time curves, the as-built sample had a lower creep rate in the transient stage, yielding a lower minimum creep rate compared with the MGD with an identical time-to-rupture. This was despite the higher stress applied to the as-built sample compared to the MGD. Thus, the LPBF sample exhibited a shorter time-to-rupture against its minimum creep rate, suggesting sudden acceleration and creep failure. Fig. 7 (k) shows the LPBF-sample creep rate vs. time curves under 100 MPa at 923 K compared with MGD with an identical time-to-rupture and MGD with identical applied stress. Even though the LPBF-sample creep testing is in progress, a minimum creep rate of approximately $10^{-6}\,h^{-1}$ has been obtained. In contrast, the MGD minimum creep rate under the same creep conditions was approximately $10^{-4}\,h^{-1}$, suggesting a LPBF-sample creep resistance two orders of magnitude higher than that of the MGD. Comparing the creep rate vs. strain curves, the strain at the acceleration-creep onset was lower than that of the MGD.

Fig. 8(a)–(c) show creep-ruptured specimens crept at 923 K. As expected from Fig. 7(c), significant necking is apparent. Fig. 8(d) and (e) show the sample fractography and an enlargement of the square box labeled "e" in Fig. 8(d), respectively. Dimples are apparent throughout the fracture surface, indicating ductile fracturing.

3.3. Microstructural changes during creep deformation

Fig. 9 shows the Vickers hardness of creep-ruptured specimen gauge and grip portions vs. the time-to-rupture. The gauge-portion hardness was measured ~10 mm from the fracture surface, where necking was negligible. The as-built sample hardness was closer to those of the as-normalized or as-quenched martensite in the conventional modified 9Cr-1Mo steels (HV ~ 400 [34,35]) than that of the tempered martensite (HV ~ 220–235 [17,36]), as the as-built sample martensite was untempered. Dislocation strengthening in the δ-ferrite likely contributed to the enhanced hardness of the as-built sample (Fig. 3). Fig. 9 includes the hardness line of an LPBF sample tempered at 1053 K for 0.5 h for reference [14]. Tempering reduces the hardness to that of tempered conventional modified 9Cr-1Mo steels [14]. For the creep-ruptured specimens, the gauge- and grip-portion hardness decreased continuously with time-to-rupture. This is attributed to dislocation recovery, coarsening of the lath martensite structure, and precipitate [17]. The gauge-portion hardness reduction was considerably more significant, suggesting that applied stress or deformation enhances microstructural degradation during creep exposure.

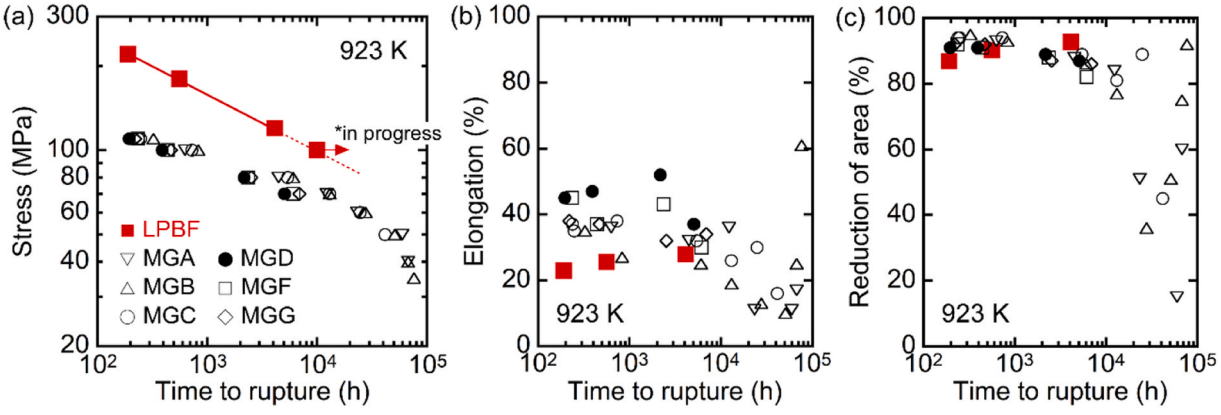

Fig. 6. (a)—(c) Stress, elongation, and reduction of area, respectively, vs, time-to-rupture of as-built sample. The T91-steel (MGA—MGG heats) reference data reported in the NIMS Creep Data Sheet [15] are plotted for comparison.

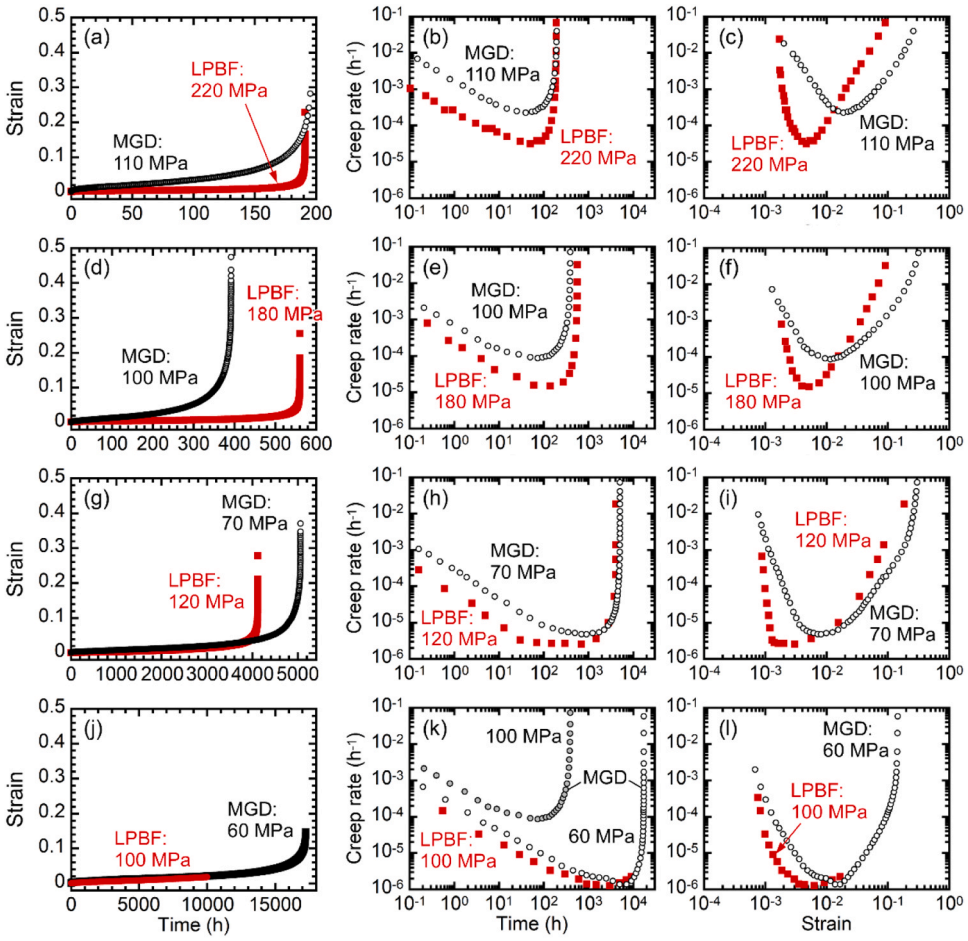

Fig. 7. (a)(d)(g)(j) strain vs. time curves, (b)(e)(h)(k) creep rate vs. time curves, and (c)(f)(i)(l) creep rate vs. strain curves of as-built sample crept at 923 K under (a)—(c) 220, (d)—(f) 180, (g)—(i) 120, and (j)—(l) 100 MPa (in progress). The curves for MGD with identical time-to-rupture are presented for comparison.

Fig. 10(a) shows the IQ + IPF map obtained near the fracture surface of a specimen that ruptured after 4120.8 h at 923 K under 120 MPa. The orientation parallel to the build direction is shown in the IPF maps. The grains were significantly elongated in the longitudinal direction. The columnar grain structure of the as-built microstructure disappeared completely. In addition, creep voids were apparent in the map, indicated by low IQ values. Fig. 10(b)–(d) show stereographic projections of the 001, 111, and 110 planes, which indicate a strong texture formation in the <110>//stress direction near the fracture surface, where necking was significant. This texture is identical to that of the α-fiber typically observed in rolled bcc steels [37]. Fig. 10(e) shows the IPF map of the box labeled “e” in Fig. 10(a). Black line indicates the high angle grain boundaries (HAGBs) with misorientation angles greater than 15 degrees. The grains 1 and 2 indicated by arrows are surrounded by HAGBs. Fig. 10(f) shows the standard stereographic triangle representing the crystallographic orientation along stress direction of the grains 1 and 2. This revealed these grains are not oriented in the <110>//stress direction. Fig. 10(g) shows the grain orientation spread (GOS) map. The grains which GOS was greater than 5 degrees are drawn by white in the map. This revealed that the GOS value of the grains 1 and 2 are significantly lower than the other grains. Consequently, these grains are considered to be recrystallized grains generated in the latter creep-testing stage driven by the severe plastic deformation.

Fig. 10(h) is an IQ + IPF map taken ~7 mm from the fracture surface, where necking was less significant. In contrast to Fig. 10(a), the columnar grain structure of the as-built microstructure was preserved, and no creep voids were apparent. Furthermore, the texture of the <001>//build direction observed in the as-built condition was maintained (Fig. 10(g)—(i)), suggesting an insignificant microstructural change (coarsening or dynamic recrystallization) in the δ-ferrite grains in the homogeneously deformed region. The orientation information of martensite grains is apparent in Fig. 10(h) than that of the as-built sample (Fig. 2(b)) because of the improved IQ value, which is related to crystallographic defects such as dislocations and plastic strain [38]. Fig. 10(j) shows an enlargement of the square box labeled “l” in Fig. 10 (h). Even though a hierarchical lath martensitic structure is observed in the as-built sample (Fig. 2(f)), equiaxed fine grains are observed in the martensite region of the creep ruptured sample. These suggests that significant dynamic recovery occurred in the martensite region, consistent with the reduced hardness of the creep-ruptured specimens (Fig. 9).

Fig. 11 shows STEM-BF images and EDS maps for Cr, V, and Nb. The thin foil for STEM was sampled from the gauge portion, sufficiently far from the fracture surface and independent of necking. No precipitates were recognized in the as-built sample martensite (Fig. 4). However, $M_{23}C_6$- and MX-phase precipitation occurred in the martensite within 200 h at 923 K (Fig. 11(a)–(d)). They nucleated at the prior austenite, packet, block, and lath boundaries. This microstructural change is identical to that observed in the martensite of conventional modified 9Cr-1Mo steels. Comparison of Figs. 4(c), 11(a)—(d) and (e)—(h) indicates lath width coarsening from hundreds of nanometers to approximately 1 μm (dynamic recovery of martensite) and coarsening/reduced number density of the $M_{23}C_6$ and MX phases during creep exposure. Those of the $M_{23}C_6$ phase are considerably more significant than those of the MX phase. The number density of the $M_{23}C_6$ phase in creep-ruptured samples ruptured after 191. 0 and 4120.8 h, as measured from the Cr

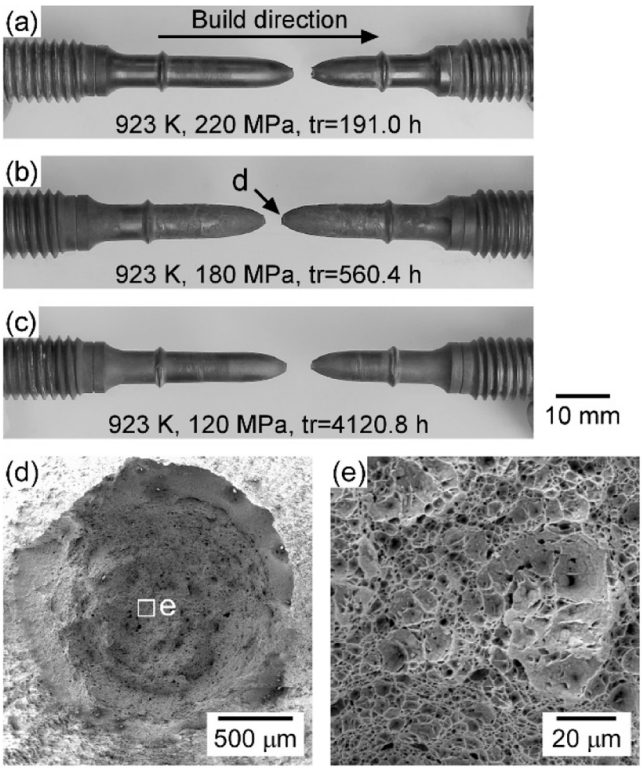

Fig. 8. Creep-ruptured specimens crept at 923 K under (a) 220, (b) 180, and (c) 120 MPa. SEM images of creep-ruptured specimen fracture surfaces after 560.4 h creep at 923 K under 180 MPa.

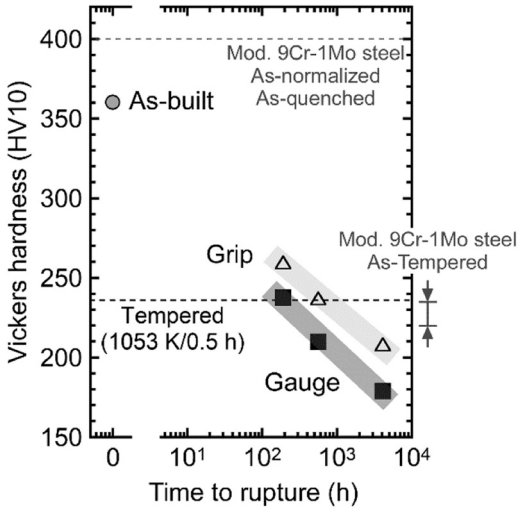

Fig. 9. Vickers hardness of creep-ruptured specimen gauge and grip portions vs. time-to-rupture. The hardness of the as-built and tempered samples manufactured using the same parameter [14] and that of the conventional modified 9Cr-1Mo steels [17,34–36] are presented for comparison.

maps (Fig. 11(b) and (f)) was 4.6 and 2.1 μm^{-2}, respectively. These values are higher than those observed in the as-tempered MGB heat (approximately 2 μm^{-2}) and that ruptured after crept for 27727.9 h at 923 K (approximately 0.5 μm^{-2}) [36], suggesting an enhanced contribution of precipitation strengthening in the martensite of the LPBF sample compared to the conventional steel.

Fig. 11(i)—(l) show the δ-ferrite microstructure. In contrast to the martensite region, as suggested by the EBSD results, the δ-ferrite coarsening or dynamic recrystallization during creep deformation was negligible. The $M_{23}C_6$-phase area fraction was considerably smaller than that of the martensite region. Notably, although Cr enrichment is almost unrecognizable in Fig. 11(j), that at the grain boundary was confirmed by higher-magnification observation, suggesting $M_{23}C_6$-phase precipitation, as observed in the as-built sample (Fig. 4(b)). Further, the MX phase densely precipitated at the δ-ferrite grain boundary, with the grain boundary having a high area fraction of precipitates. MX-phase precipitation in the grain interior was also observed. The δ-ferrite dislocation density was likely reduced from that of the as-built sample. The cellular structures of the dislocations observed in the as-built sample were not confirmed in this sample, suggesting recovery in the δ-ferrite during creep exposure.

Fig. 12(a) and (b) show STEM-BF images and STEM-EDS maps for Si taken from the martensite of a creep-ruptured specimen that ruptured after 4120.8 h creep under 120 MPa at 923 K. Coarse $M_{23}C_6$-phase precipitation was observed. Dispersion of the fine Si-oxide phase was confirmed (see arrowheads). Fig. 12(c) is the STEM-BF image of the δ-ferrite of the same specimen. The number of fine precipitates in the grain interiors was confirmed. Interactions between the dislocations and precipitates were observed, suggesting that these precipitates contributed to precipitation strengthening. Some were identified as the MX phase (Fig. 12(c)), and others were likely the Si-oxide phase (Fig. 12(d)). The oxide was considerably smaller than the $M_{23}C_6$ and MX phases.

4. Discussion

In conventional high-Cr steels with martensite matrix, δ-ferrite phase formation is detrimental to the creep strength [39]. However, LPBF samples with ~40 % δ-ferrite volume fraction exhibit significantly enhanced creep strength (Fig. 6(a)). The δ-ferrite formed through the conventional process is stabilized by ferrite-former segregation in the final stage of the solidification process; thus, the δ-ferrite phase in conventional high-Cr steels contains more Cr and Mo (or W) than the surrounding martensite matrix [39–41]. The chemical composition gradients between the δ-ferrite and martensite enhance the microstructural degradation of the adjacent martensite and reduce the creep strength [42]. However, this detrimental effect does not occur for an LPBF sample because no substitutional ferrite-former segregation is observed between the δ-ferrite and martensite [14].

Kimura et al. [43] investigated the long-term creep properties of 0.5Cr-0.5Mo steel with different initial microstructures controlled by various heat treatments. The creep strength differed from the initial microstructure even for identical chemical compositions. Their annealed ferrite + pearlite microstructure (initial-microstructure HV = 114) had superior creep strength to that with martensite (initial-microstructure HV = 408) because of the lower mobile dislocation density in the ferrite than in the martensite in the initial microstructure. Thus, the high hardness of the initial microstructure barely contributes to the as-built sample creep strength. Therefore, the lower creep rate of the LPBF sample in the transient stage shown in Fig. 7 is attributed to its δ-ferrite-containing microstructure, not the high hardness of the as-built microstructure (Fig. 9). However, it was suggested that high hardness in the initial microstructure results in the steeper stress vs. time-to-rupture slope in Fig. 6(a) by enhancing the microstructure degradation during creep deformation.

The results presented by Kimura et al. [43] also suggested potential improvement of steel creep strength using a ferrite rather than a martensite matrix. They demonstrated this using a series of 15Cr steels strengthened with precipitates in a ferrite matrix [44–46]. However, 9Cr steels with ferrite matrices are unavailable because of their excellent hardenability. Therefore, higher Cr concentrations, exceeding the Fe—Cr-system γ loop, have been used in alloy designs to obtain a ferrite-matrix microstructure. In contrast, in LPBF, the ferrite phase is obtained by suppressing the diffusional transformation from the δ-ferrite to γ during the 9Cr-steel solidification through the rapid cooling rate (of the order of 10^6 K/s) [13]. Thus, LPBF may provide a novel

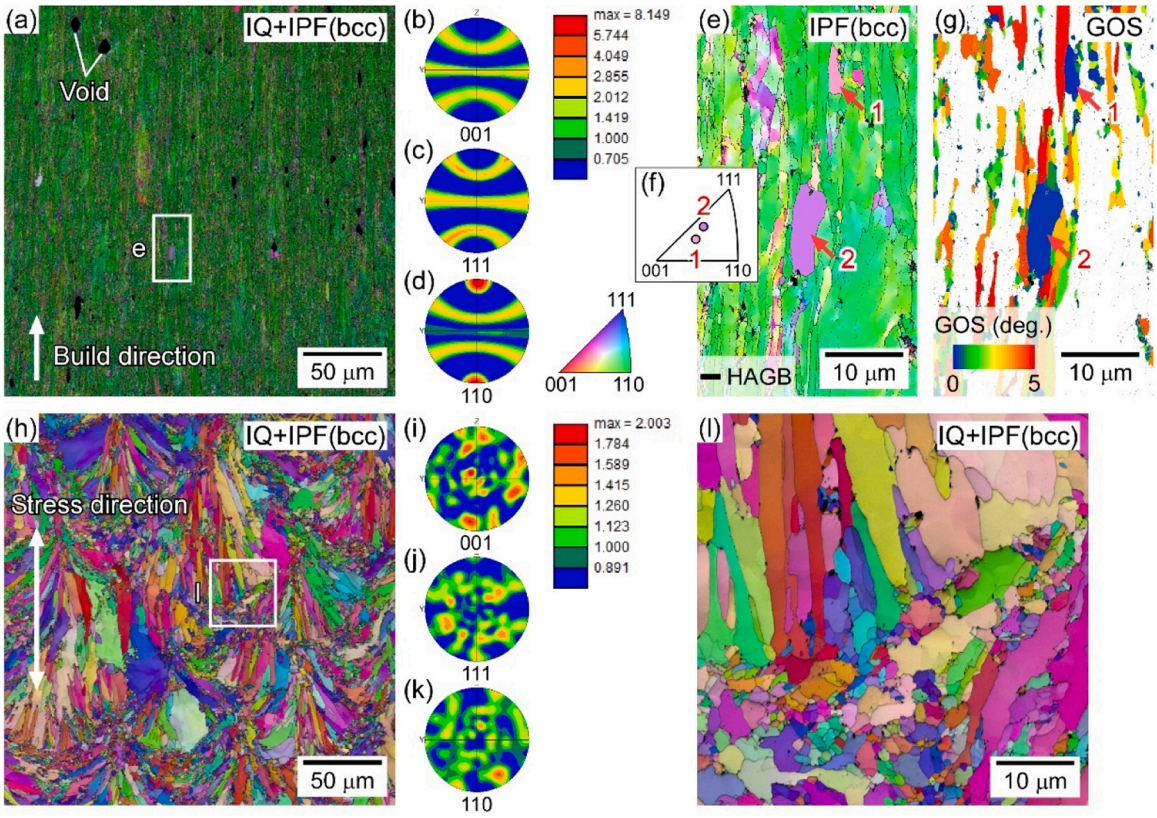

Fig. 10. (a)(h)(l) Cross-sectional IQ + IPF map, stereographic projections of (b)(i) 001, (c)(j) 111, (d)(k) 110 of bcc grains, (e) IPF + high angle grain boundary (HAGB) map, (f) crystallographic orientation along stress direction of grain 1 and 2 in (e), and (g) grain orientation spread (GOS) map of creep-ruptured specimens ruptured after 4120.8 h at 923 K under 120 MPa. (a)—(g) Near and (h)—(l) ~7 mm from fracture surface.

microstructural control process for steels and alloys, overcoming diffusional controlled transformation kinetics, which is unavoidable in conventional heat-treatment processes.

The $M_{23}C_6$ and MX phases are the major precipitates in the lath martensite of conventionally manufactured modified 9Cr-1Mo steels [47–49]. However, the $M_{23}C_6$-phase coarsening rate is considerably higher than that of the MX phase in 9Cr steel [50–52]. Taneike et al. [53,54] demonstrated that 9Cr-steel creep strength improves significantly with nanosized MX-phase dispersion instead of $M_{23}C_6$-phase precipitation by reducing the carbon concentration. In low carbon 9Cr steel, the MX phase densely precipitates on the prior austenite, packet, block, and lath boundaries [53,54]. The MX phase has sluggish coarsening kinetics; thus, its contribution to the precipitation strengthening is expected to exceed that of the $M_{23}C_6$ phase [53,54]. The microstructural characterization performed herein revealed dense MX-phase precipitation in the δ-ferrite grain boundary (Fig. 11(k)), suggesting that δ-ferrite grain boundary was stabilized by this MX phase. Thus, the δ-ferrite grain coarsening during creep deformation was disturbed. Additionally, these MX phases likely contribute to grain-boundary precipitation strengthening [55,56]. Therefore, the MX-phase precipitation on the grain boundary is identified as a microstructural factor that potentially enhances the LPBF-manufactured steel creep strength.

According to Taneike et al. [54], the $M_{23}C_6$- and MX-phase precipitation kinetics in 9Cr steel are influenced by carbon concentration. Although no partitioning of the substitutional alloying elements between the δ-ferrite and martensite was recognized in the as-built sample [14], carbon depletion in the δ-ferrite (carbon enrichment in the martensite) was confirmed in the as-built sample (Fig. 5). This suggests that carbon atoms are partitioned into the γ phase transformed at the heat-affected zone during LPBF, and the enriched carbon atoms are preserved in the resulting martensite.

Furthermore, the Si oxide dispersed in the δ-ferrite and martensite grain interiors likely contributed to the LPBF-sample creep strength (Fig. 12). That is, oxide dispersion strengthening is another microstructural factor that potentially enhances LPBF-manufactured steel creep strength. Because the oxides remain extremely fine (~10 nm), even after creep exposure, they likely contribute to the creep strength, even in the longer term. However, the contribution of oxide dispersion strengthening is expected to be less than the other factors by considering the smaller amount of O in the steel (0.01 mass%) is than that of the 9Cr ODS steels (0.1–0.2 mass%) [57]. This minor contribution of the oxide is evident by the identical hardness of the tempered and normalized + tempered LPBF samples [14] compared with that of the conventional modified 9Cr-1Mo steels [17,36].

Kushima et al. [58] discovered the preferential recovery at the vicinity of prior γ grain boundary of creep ruptured T91 steel in the long-term side. This microstructural inhomogeneity promotes the localization of creep deformation, which lowers the amount of strain at the accelerating-creep onset and creep rupture elongation due to the reduced contribution of the grain interior deformation to the overall creep strain of the specimen [58]. As suggested in Figs. 10 and 11, the δ-ferrite microstructural stability exceeded that in the martensite in the LPBF-sample duplex microstructure, and recovery preferentially occurred in the martensite during creep deformation. Thus, the creep deformation was inhomogeneous and locally concentrated at the martensite, further enhancing its dynamic recovery. This inhomogeneity owing to the duplex microstructure explains the smaller strain at the acceleration-creep onset and creep rupture elongation of the LPBF sample shown in Figs. 6 and 7.

It was revealed that the creep strength of modified 9Cr-1Mo steel was successfully improved via unique microstructure control through LPBF. However, anisotropy in the creep strength and ductility has been reported in various alloys manufactured through LPBF [32,59–64]. Since only the creep properties of vertical build direction were investigated in

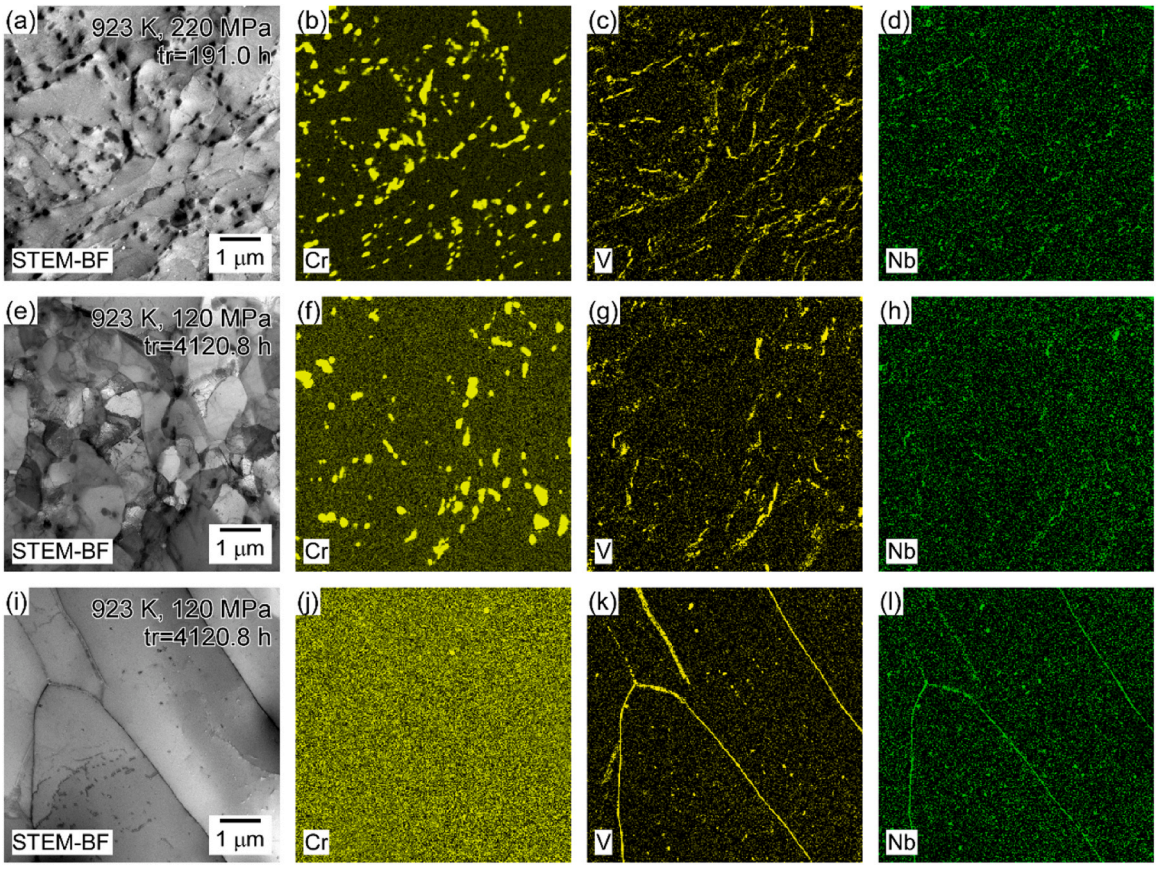

Fig. 11. (a)(e)(i) STEM-BF images and EDS maps for (b)(f)(j) Cr, (c)(g)(k) V, and (d)(h)(l) Nb of creep-ruptured samples ruptured after (a)—(d) 191.0 h under 220 MPa and (e)—(l) 4120.8 h under 120 MPa at 923 K. (a)—(h) Martensite, (i)—(l) δ-ferrite.

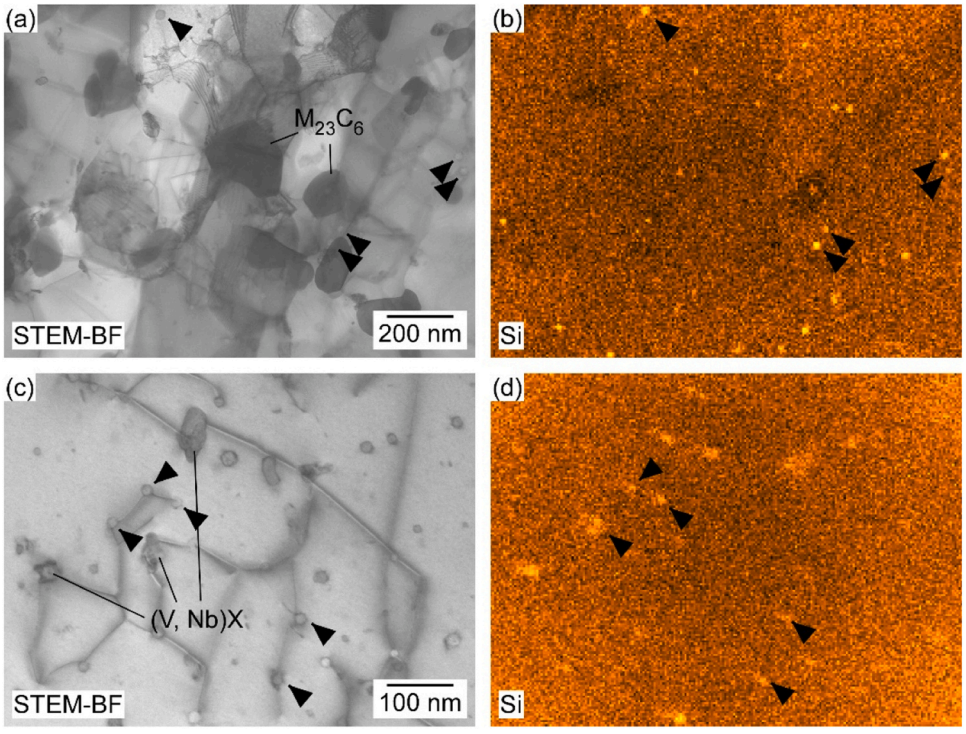

Fig. 12. (a)(c) STEM-BF images and (b)(d) STEM-EDS maps for Si of creep-ruptured specimen ruptured after 4120.8 h under 120 MPa at 923 K. (a)(b) Martensite and (c)(d) δ-ferrite.

this study, it is necessary to examine the effect of build direction in future work.

5. Conclusions

The microstructural and creep deformation behaviors of LPBF-manufactured modified 9Cr-1Mo steel were investigated. The as-built microstructure comprised δ-ferrite and martensite. A cellular dislocation structure with segregation was observed in the δ-ferrite grains. The creep strength significantly exceeded that of conventionally manufactured steel. The LPBF-sample creep ductility was comparable to those of conventional steels. Based on microstructural characterization, the superior intrinsic creep resistance of the δ-ferrite phase compared to that of the martensite and the microstructural stability of the δ-ferrite due to the dense precipitation of the MX phase at the grain boundaries were suggested as the LPBF-sample strengthening microstructural factors. The beneficial δ-ferrite phase only arises through the rapid solidification of the LPBF process, which permits suppression of the solid-state phase transformation during the solidification. Therefore, this result demonstrates the potential of the LPBF process as a novel microstructural control process.

CRediT authorship contribution statement

Kota Sawada: Writing – review & editing, Resources, Funding acquisition, Conceptualization. **Tomotaka Hatakeyama:** Writing – original draft, Visualization, Methodology, Investigation, Funding acquisition, Formal analysis, Data curation, Conceptualization. **Masahiro Kusano:** Writing – review & editing, Resources, Investigation. **Makoto Watanabe:** Writing – review & editing, Supervision, Resources.

Declaration of Competing Interest

The authors declare that they have no known competing financial interests or personal relationships that could have appeared to influence the work reported in this paper.

Data Availability

Data will be made available on request.

Acknowledgements

The authors thank Mr. Masaru Suzuki for his support with additive manufacturing; Mr. Mitsuaki Nishio for his support with chemical analysis, Mr. Yasushi Taniuchi, Dr. Kaoru Sekido, and Mr. Takehiro Nojima for their support with creep testing; and Dr. Toru Hara, Mr. Taku Moronaga, Ms. Yuka Hara, and Ms. Akiko Nakamura for their support with microstructural observations (all at NIMS). This study was supported by Chubu Electric Power and the Japan Boiler Association.

References

[1] K. Hagihara, T. Nakano, Control of anisotropic crystallographic texture in powder bed fusion additive manufacturing of metals and ceramics—a review, JOM 74 (2022) 1760–1773, https://doi.org/10.1007/s11837-021-04966-7.
[2] F. Masuyama, Advances in physical metallurgy and processing of steels. History of power plants and progress in heat resistant steels, ISIJ Int. 41 (2001) 612–625, https://doi.org/10.2355/isijinternational.41.612.
[3] R.L. Klueh, A.T. Nelson, Ferritic/martensitic steels for next-generation reactors, J. Nucl. Mater. 371 (2007) 37–52, https://doi.org/10.1016/j.jnucmat.2007.05.005.
[4] Y. Shi, Z. Lu, Y. Ren, G. Yang, Microstructure and tensile properties of laser engineered net shaped reduced activation ferritic/martensitic steel, Mater. Charact. 144 (2018) 554–562, https://doi.org/10.1016/j.matchar.2018.08.010.
[5] W. Zhong, N. Sridharan, D. Isheim, K.G. Field, Y. Yang, K. Terrani, L. Tan, Microstructures and mechanical properties of a modified 9Cr ferritic-martensitic steel in the as-built condition after additive manufacturing, J. Nucl. Mater. 545 (2021) 152742, https://doi.org/10.1016/j.jnucmat.2020.152742.
[6] L. Tan, W. Zhong, Y. Yang, K.G. Field, N. Sridharan, A.T. Nelson, Creep behavior of an additively manufactured 9Cr steel in the as-built, J. Nucl. Mater. 570 (2022) 153943, https://doi.org/10.1016/j.jnucmat.2022.153943.
[7] N. Ordás, L.C. Ardila, I. Iturriza, F. Garcianda, P. Álvarez, C. García-Rosales, Fabrication of TBMs cooling structures demonstrators using additive manufacturing (AM) technology and HIP, Fusion Eng. Des. 96– 97 (2015) 142–148, https://doi.org/10.1016/j.fusengdes.2015.05.059.
[8] B. Huang, Y. Zhai, S. Liu, X. Mao, Microstructure anisotropy and its effect on mechanical properties of reduced activation ferritic/martensitic steel fabricated by selective laser melting, J. Nucl. Mater. 500 (2018) 33–41, https://doi.org/10.1016/j.jnucmat.2017.12.011.
[9] O. El-Atwani, B.P. Eftink, C.M. Cady, D.R. Coughlin, M.M. Schneider, S.A. Maloy, Enhanced mechanical properties of additive manufactured Grade 91 steel, Scr. Mater. 199 (2021) 113888, https://doi.org/10.1016/j.scriptamat.2021.113888.
[10] B.P. Eftink, D.A. Vega, O.El Atwani, D.J. Sprouster, Y.S.J. Yoo, T.E. Steckley, E. Aydogan, C.M. Cady, M. Al-Sheikhly, T.J. Lienert, S.A. Maloy, Tensile properties and microstructure of additively manufactured Grade 91 steel for nuclear applications, J. Nucl. Mater. 544 (2021) 152723, https://doi.org/10.1016/J.JNUCMAT.2020.152723.
[11] M. Sau, E.D. Hintsala, Y. Chen, D.D. Stauffer, S.A. Maloy, B.P. Eftink, T.J. Lienert, N.A. Mara, High-throughput nanoindentation mapping of additively manufactured T91 steel, Jom 74 (2022) 1469–1476, https://doi.org/10.1007/s11837-022-05189-0.
[12] M.G. Jiang, Z.W. Chen, J.D. Tong, C.Y. Liu, G. Xu, H.B. Liao, P. Wang, X.Y. Wang, M. Xu, C.S. Lao, Strong and ductile reduced activation ferritic/martensitic steel additively manufactured by selective laser melting, Mater. Res. Lett. 7 (2019) 426–432, https://doi.org/10.1080/21663831.2019.1631224.
[13] F. Villaret, X. Boulnat, P. Aubry, J. Zollinger, D. Fabrègue, Y. de Carlan, Modelling of delta ferrite to austenite phase transformation kinetics in martensitic steels: application to rapid cooling in additive manufacturing, Mater. (Oxf.) 18 (2021) 101157, https://doi.org/10.1016/J.MTLA.2021.101157.
[14] T. Hatakeyama, K. Sawada, M. Suzuki, M. Watanabe, Microstructure development of modified 9Cr-1Mo steel during laser powder bed fusion and heat treatment, Addit. Manuf. 61 (2023) 103350, https://doi.org/10.1016/J.ADDMA.2022.103350.
[15] NIMS Creep Data Sheet, No. 43A, National Institute for Materials Science (2014).
[16] H. KUSHIMA, K. KIMURA, F. ABE, Degradation of Mod.9Cr-1Mo steel during long-term creep deformation, Tetsu-to-Hagane 85 (1999) 841–847, https://doi.org/10.2355/tetsutohagane1955.85.11_841.
[17] K. Sawada, H. Kushima, M. Tabuchi, K. Kimura, Microstructural degradation of Gr.91 steel during creep under low stress, Mater. Sci. Eng. A 528 (2011) 5511–5518, https://doi.org/10.1016/j.msea.2011.03.073.
[18] K. KIMURA, H. KUSHIMA, F. ABE, Improvement of creep life prediction of high Cr ferritic creep resistant steels by region partitioning method of stress vs. time to rupture diagram, J. Soc. Mater. Sci. Jpn. 52 (2003) 57–62, https://doi.org/10.2472/jsms.52.57.
[19] K. Maruyama, J. Nakamura, N. Sekido, K. Yoshimi, Causes of heat-to-heat variation of creep strength in grade 91 steel, Mater. Sci. Eng.: A 696 (2017) 104–112, https://doi.org/10.1016/j.msea.2017.04.050.
[20] K. Sawada, K. Kimura, F. Abe, Y. Taniuchi, K. Sekido, T. Nojima, T. Ohba, H. Kushima, H. Miyazaki, H. Hongo, T. Watanabe, Catalog of NIMS creep data sheets, Sci. Technol. Adv. Mater. 20 (2019) 1131–1149, https://doi.org/10.1080/14686996.2019.1697616.
[21] Boilar and Pressure Vessel Code, Section II-A, SA213/SA213M Grade, T91 Type 1,, ASME (2019).
[22] I. Gutierrez-Urrutia, S. Zaefferer, D. Raabe, Electron channeling contrast imaging of twins and dislocations in twinning-induced plasticity steels under controlled diffraction conditions in a scanning electron microscope, Scr. Mater. 61 (2009) 737–740, https://doi.org/10.1016/j.scriptamat.2009.06.018.
[23] I. Gutierrez-Urrutia, S. Zaefferer, D. Raabe, The effect of grain size and grain orientation on deformation twinning in a Fe-22wt% Mn-0.6wt% C TWIP steel, Mater. Sci. Eng.: A 527 (2010) 3552–3560, https://doi.org/10.1016/j.msea.2010.02.041.
[24] I. Gutierrez-Urrutia, D. Raabe, Dislocation and twin substructure evolution during strain hardening of an Fe-22 wt% Mn-0.6 wt% C TWIP steel observed by electron channeling contrast imaging, Acta Mater. 59 (2011) 6449–6462, https://doi.org/10.1016/j.actamat.2011.07.009.
[25] T. Voisin, J.B. Forien, A. Perron, S. Aubry, N. Bertin, A. Samanta, A. Baker, Y. M. Wang, New insights on cellular structures strengthening mechanisms and thermal stability of an austenitic stainless steel fabricated by laser powder-bed-fusion, Acta Mater. 203 (2021), https://doi.org/10.1016/j.actamat.2020.11.018.
[26] F. Yan, W. Xiong, E. Faierson, G.B. Olson, Characterization of nano-scale oxides in austenitic stainless steel processed by powder bed fusion, Scr. Mater. 155 (2018) 104–108, https://doi.org/10.1016/j.scriptamat.2018.06.011.
[27] P. Deng, M. Karadge, R.B. Rebak, V.K. Gupta, B.C. Prorok, X. Lou, The origin and formation of oxygen inclusions in austenitic stainless steels manufactured by laser powder bed fusion, Addit. Manuf. 35 (2020) 101334, https://doi.org/10.1016/j.addma.2020.101334.
[28] K. Saeidi, L. Kvetková, F. Lofaj, Z. Shen, Austenitic stainless steel strengthened by the in situ formation of oxide nanoinclusions, RSC Adv. 5 (2015) 20747–20750, https://doi.org/10.1039/C4RA16721J.
[29] F. He, C. Wang, B. Han, G. Yeli, X. Lin, Z. Wang, L. Wang, J.J. Kai, Deformation faulting and dislocation-cell refinement in a selective laser melted 316L stainless steel, Int J. Plast. 156 (2022), https://doi.org/10.1016/j.ijplas.2022.103346.

[30] K.M. Bertsch, G. Meric de Bellefon, B. Kuehl, D.J. Thoma, Origin of dislocation structures in an additively manufactured austenitic stainless steel 316L, Acta Mater. 199 (2020) 19–33, https://doi.org/10.1016/j.actamat.2020.07.063.
[31] S. Sanchez, G. Gaspard, C.J. Hyde, I.A. Ashcroft, R. G.A., A.T. Clare, The creep behaviour of nickel alloy 718 manufactured by laser powder bed fusion, Mater. Des. 204 (2021) 109647, https://doi.org/10.1016/j.matdes.2021.109647.
[32] Y.L. Kuo, S. Horikawa, K. Kakehi, Effects of build direction and heat treatment on creep properties of Ni-base superalloy built up by additive manufacturing, Scr. Mater. 129 (2017) 74–78, https://doi.org/10.1016/j.scriptamat.2016.10.035.
[33] L.A. Ávila Calderón, B. Rehmer, S. Schriever, A. Ulbricht, L. Agudo Jácome, K. Sommer, G. Mohr, B. Skrotzki, A. Evans, Creep and creep damage behavior of stainless steel 316L manufactured by laser powder bed fusion, Mater. Sci. Eng.: A 830 (2022) 142223, https://doi.org/10.1016/j.msea.2021.142223.
[34] K. Sawada, K. Miyahara, H. Kushima, K. Kimura, S. Matsuoka, Contribution of microstructural factors to hardness change during creep exposure in Mod.9Cr-1Mo steel, ISIJ Int. 45 (2005) 1934–1939, https://doi.org/10.2355/isijinternational.45.1934.
[35] K. Watanabe, S. Ida, K. Yoshimi, Influence of carbides precipitated by low-temperature tempering on the room-temperature mechanical properties of grade 91 steel, ISIJINT-2022-213. ISIJ Int. 62 (2022) https://doi.org/10.2355/isijinternational.ISIJINT-2022-213.
[36] K. Sawada, K. Sekido, K. Kimura, K. Arisue, M. Honda, N. Komai, N. Fukuzawa, T. Ueno, N. Shimohata, H. Nakatomi, K. Takagi, T. Kimura, K. Nomura, K. Kubushiro, Effect of initial microstructure on creep strength of ASME grade T91 steel, ISIJ Int. 60 (2020) 382–391, https://doi.org/10.2355/isijinternational.ISIJINT-2019-358.
[37] M. Hölscher, D. Raabe, K. Lücke, Rolling and recrystallization textures of bcc steels, Steel Res. 62 (1991) 567–575, https://doi.org/10.1002/srin.199100451.
[38] J. Wu, P.J. Wray, C.I. Garcia, M. Hua, A.J. Deardo, Image quality analysis: a new method of characterizing microstructures, ISIJ Int. 45 (2005) 254–262, https://doi.org/10.2355/ISIJINTERNATIONAL.45.254.
[39] S. Kobayashi, K. Sawada, T. Hara, H. Kushima, K. Kimura, The formation and dissolution of residual δ ferrite in ASME Grade 91 steel plates, Mater. Sci. Eng. A 592 (2014) 241–248, https://doi.org/10.1016/j.msea.2013.10.058.
[40] S. Li, Z. Eliniyaz, L. Zhang, F. Sun, Y. Shen, A. Shan, Microstructural evolution of delta ferrite in SAVE12 steel under heat treatment and short-term creep, Mater. Charact. 73 (2012) 144–152, https://doi.org/10.1016/j.matchar.2012.08.009.
[41] G. Chakraborty, J. Ganesh Kumar, P. Vasantharaja, C.R. Das, S.K. Albert, K. Laha, Effect of delta ferrite on microstructure and mechanical properties of high-chromium martensitic steel, J. Mater. Eng. Perform. 28 (2019) 876–885, https://doi.org/10.1007/s11665-019-3862-8.
[42] K. Kimura, K. Sawada, H. Kushima, Y. Toda, Long-term creep strength of creep strength enhanced ferritic steels. in: Challenges of Power Engineering and Environment, Springer, Berlin Heidelberg, Berlin, Heidelberg, 2007, pp. 1059–1065, https://doi.org/10.1007/978-3-540-76694-0_196.
[43] K. KIMURA, H. KUSHIMA, E. BABA, T. SHIMIZU, Y. ASAI, F. ABE, K. YAGI, Effect of initial microstructure on long term creep strength of a low alloy ferritic steel, Tetsu-to-Hagane 86 (2000) 542–549, https://doi.org/10.2355/tetsutohagane1955.86.8_542.
[44] K. Kimura, K. Seki, Y. Toda, F. Abe, Development of high strength 15Cr ferritic creep resistant steel with addition of tungsten and cobalt, ISIJ Int. 41 (2001), https://doi.org/10.2355/isijinternational.41.Suppl_S121.
[45] Y. Toda, M. Iijima, H. Kushima, K. Kimura, F. ABE, Effects of Ni and heat treatment on long-term creep strength of precipitation strengthened 15cr ferritic heat resistant steels, ISIJ Int. 45 (2005) 1747–1753, https://doi.org/10.2355/isijinternational.45.1747.
[46] Y. Toda, H. Tohyama, H. Kushima, K. Kimura, F. Abe, Improvement in creep strength of precipitation strengthened 15Cr ferritic steel by controlling carbon and nitrogen contents, JSME Int. J. Ser. A 48 (2005) 35–40, https://doi.org/10.1299/jsmea.48.35.
[47] K. Maruyama, K. Sawada, J.I. Koike, Strengthening mechanisms of creep resistant tempered martensitic steel, ISIJ Int. 41 (2001) 641–653, https://doi.org/10.2355/isijinternational.41.641.
[48] K. Sawada, H. Kushima, T. Hara, M. Tabuchi, K. Kimura, Heat-to-heat variation of creep strength and long-term stability of microstructure in Grade 91 steels, Mater. Sci. Eng.: A 597 (2014) 164–170, https://doi.org/10.1016/j.msea.2013.12.088.
[49] C.G. Panait, A. Zielińska-Lipiec, T. Koziel, A. Czyrska-Filemonowicz, A.-F. Gourgues-Lorenzon, W. Bendick, Evolution of dislocation density, size of subgrains and MX-type precipitates in a P91 steel during creep and during thermal ageing at 600C for more than 100,000h, Mater. Sci. Eng.: A 527 (2010) 4062–4069, https://doi.org/10.1016/j.msea.2010.03.010.
[50] J. Hald, L. Korcakova, Precipitate stability in creep resistant ferritic steels-experimental investigations and modelling, ISIJ Int. 43 (2003) 420–427, https://doi.org/10.2355/isijinternational.43.420.
[51] K. Sawada, K. Kubo, F. Abe, Creep behavior and stability of MX precipitates at high temperature in 9Cr–0.5Mo–1.8W–VNb steel, Mater. Sci. Eng.: A 319–321 (2001) 784–787, https://doi.org/10.1016/S0921-5093(01)00973-X.
[52] F. Abe, Strengthening mechanisms in creep of advanced ferritic power plant steels based on creep deformation analysis. Advanced Steels, Springer Berlin Heidelberg, Berlin, Heidelberg, 2011, pp. 409–422, https://doi.org/10.1007/978-3-642-17665-4_42.
[53] M. Taneike, F. Abe, K. Sawada, Creep-strengthening of steel at high temperatures using nano-sized carbonitride dispersions, Nature 424 (2003) 294–296, https://doi.org/10.1038/nature01740.
[54] M. Taneike, K. Sawada, F. Abe, Effect of carbon concentration on precipitation behavior of M23C6 carbides and MX carbonitrides in martensitic 9Cr steel during heat treatment, Metall. Mater. Trans. A 35 (2004).
[55] T. Mastuo, M. Ueki, M. Takeyama, R. Tanaka, Review strengthening of nickel-base superalloys for nuclear heat exchanger applications, J. Mater. Sci. 22 (1987) 1901–1907, https://doi.org/10.1007/BF01132914.
[56] M. Takeyama, Novel design principles of grain-boundary precipitation control for high-temperature alloys, Bull. Iron Steel Inst. Jpn. 23 (2018) 414–419.
[57] S. Ohtsuka, S. Ukai, M. Fujiwara, T. Kaito, T. Narita, Improvement of creep strength of 9CrODS martensitic steel by controlling excess oxygen and titanium concentrations, Mater. Trans. 46 (2005) 487–492, https://doi.org/10.2320/matertrans.46.487.
[58] H. KUSHIMA, K. KIMURA, F. ABE, Degradation of Mod.9Cr-1Mo steel during long-term creep deformation, Tetsu-to-Hagane 85 (1999) 841–847, https://doi.org/10.2355/tetsutohagane1955.85.11_841.
[59] C.-H. Yu, R.L. Peng, T.L. Lee, V. Luzin, J.-E. Lundgren, J. Moverare, Anisotropic behaviours of LPBF Hastelloy X under slow strain rate tensile testing at elevated temperature, Mater. Sci. Eng.: A 844 (2022) 143174, https://doi.org/10.1016/j.msea.2022.143174.
[60] F. Zhou, X. Hu, Y. Zhou, Z. Xu, C. Guo, G. Li, Z. Li, Y. Huang, Q. Zhu, Effects of post-heat treatment on anisotropic mechanical properties of laser additively manufactured IN718, Mater. Sci. Eng.: A 877 (2023) 145144, https://doi.org/10.1016/j.msea.2023.145144.
[61] H. Zhang, H. Liu, Y. Li, F. Chu, Q. Hu, X. Wu, H. Rao, S. Cao, Anisotropic tensile creep behavior in laser powder bed fusion manufactured Al–Mn–Mg–Sc–Zr alloy, J. Mater. Res. Technol. 28 (2024) 2071–2076, https://doi.org/10.1016/j.jmrt.2023.12.128.
[62] K. Kianinejad, R. Darvishi Kamachali, A. Khedkar, A.M. Manzoni, L.A. Jácome, S. Schriever, R. Saliwan Neumann, S. Megahed, C. Heinze, S. Kamrani, B. Fedelich, Creep anisotropy of additively manufactured Inconel-738LC: combined experiments and microstructure-based modeling, Mater. Sci. Eng.: A 907 (2024) 146690, https://doi.org/10.1016/j.msea.2024.146690.
[63] P. Sandmann, A.J. Milne, C.M. Davies, Uniaxial Creep Properties of 316L Stainless Steel Manufactured by Laser Powder Bed Fusion, in: Materials & Fabrication, vol. 5, American Society of Mechanical Engineers, 2023, https://doi.org/10.1115/PVP2023-106410.
[64] S.J. Davies, S.P. Jeffs, M.P. Coleman, R.J. Lancaster, Effects of heat treatment on microstructure and creep properties of a laser powder bed fused nickel superalloy, Mater. Des. 159 (2018) 39–46, https://doi.org/10.1016/j.matdes.2018.08.039.